Supplementary Information: Real-time 3D Temperature Reconstruction in Microwave Cancer Hyperthermia from Scarce Temperature Measurements

Authors: Rossella Gaffoglio[1], Giorgio Giordanengo[1], Marco Righero[1], Marcello Zucchi[2], Maryam Firuzalizadeh[2], Giuseppe Musacchio Adorisio[1], Aurora Bellone[2], Alberto Vallan[2], Guido Perrone[2] & Giuseppe Vecchi[2*]

Affiliations:

[1]Advanced Computing, Photonics & Electromagnetics, Fondazione LINKS, Torino, I-10138 Italy

[2]Department of Electronics and Telecommunications, Politecnico di Torino, Torino, I-10129, Italy

*Correspondence to: giuseppe.vecchi@polito.it

Supplementary Note 1 – Antenna feedings optimization

To optimize the antenna feeding coefficients of the array applicator, a SAR-based optimization approach commonly used in hyperthermia[1] was applied in both the considered scenarios (i.e., in-silico and experimental testbeds). We provide below a brief description of the method employed.

Being $\mathbf{e}_n(\mathbf{r})$ the electric field induced by the *n*th unitary excited array element acting as standalone (i.e., when all the other antennas are switched off), the total electric field generated by the array can be written as:

$$\mathbf{E}(\mathbf{r}) = \sum_{n=1}^{N_\mathrm{a}} \tilde{v}_n \, \mathbf{e}_n(\mathbf{r}), \tag{S1}$$

where N_a is the number of antennas in the array, and $\tilde{v}_n$, $n \in \{1, \dots, N_\mathrm{a}\}$, is the complex feeding coefficient of the *n*th antenna, given by:

$$\tilde{v}_n = V_0 v_n \, e^{i\varphi_n}, \tag{S2}$$

where $v_n \in (0,1]$ is a dimensionless amplitude coefficient, $\varphi_n \in [0,2\pi)$ is the phase, while V_0 is a constant amplitude normalization coefficient related to the total power P_0 delivered to the array by the following expression:

$$V_0 = \sqrt{\frac{2R_0P_0}{\sum_{n=1}^{N_\mathrm{a}} v_n^2}} \tag{S3}$$

being $R_0 = 50\ \Omega$ the reference impedance of each antenna. Once computed the standalone fields $\mathbf{e}_n(\mathbf{r})$, $n \in \{1, \dots, N_\mathrm{a}\}$ (see Eq. S1), in the electromagnetic computational solver, a particle swarm optimization (PSO) algorithm is applied to find the set of coefficients $[\tilde{v}]$ that maximize the specific absorption rate (SAR) in the tumor region, minimizing the risk of overheating in the surrounding tissues. The corresponding objective function is the target-to-hotspot SAR quotient (THQ), defined as[2]:

$$\mathrm{THQ} = \frac{\langle \mathrm{SAR}_\mathrm{target} \rangle}{\langle \mathrm{SAR}_\mathrm{V1} \rangle} \tag{S4}$$

where $\langle \mathrm{SAR}_\mathrm{target} \rangle$ indicates the average SAR in the target tumor region, and $\langle \mathrm{SAR}_\mathrm{V1} \rangle$ is the average SAR in V1, which is the 1% of the healthy volume with the highest SAR[2,3].

Supplementary Note 2 – In-silico testbed detailed description

The in-silico testbed considered in Fig. 2 of the main article has been implemented in the simulation software Sim4Life[4], using the anthropomorphic phantom Duke V3.0[5]. This anatomically accurate model was developed from high-resolution magnetic resonance imaging (MRI) data of healthy volunteers and includes a total of 305 segmented tissues with specific dielectric and thermal properties[6].

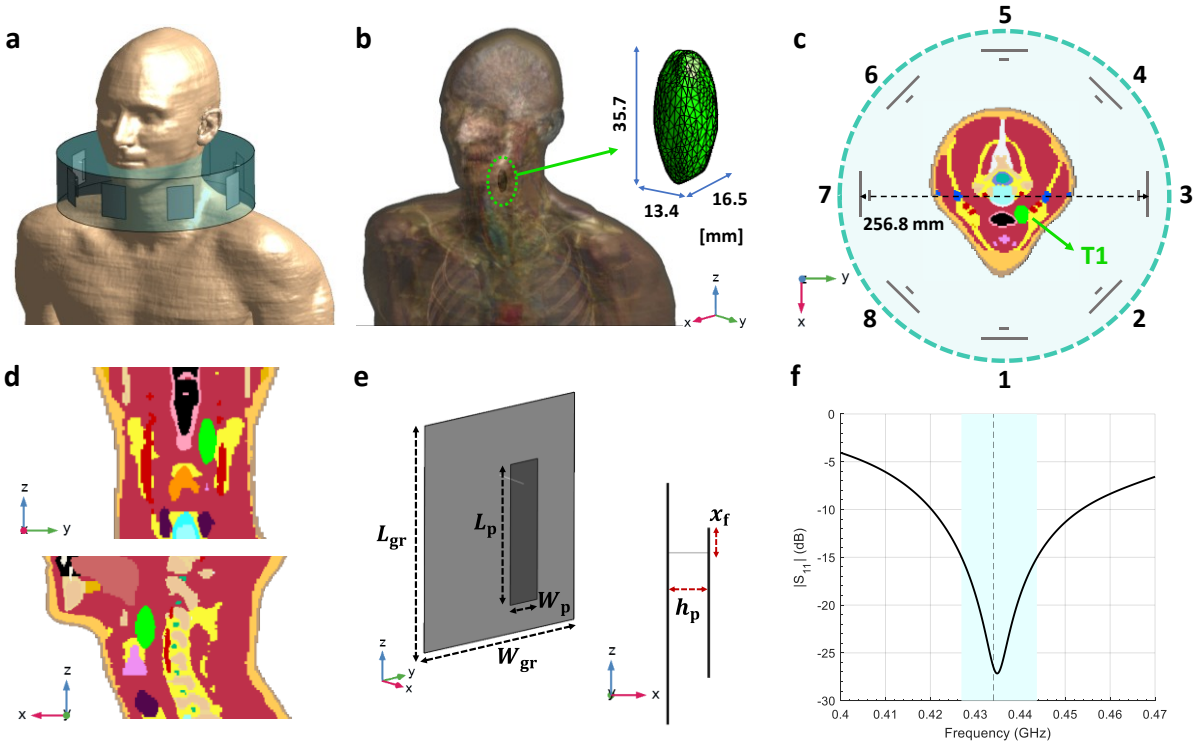

Supplementary Fig. 1 | Visualization of the in-silico testbed implemented in Sim4Life to reproduce a HT treatment. **a** Fully anthropomorphic phantom Duke V3.0 and phased array applicator immersed in the water bolus. **b** Tumor mass with irregular shape inserted in the neck of the anthropomorphic phantom, close to the larynx; the overall dimensions of the tumor mass are also reported. **c** Top view of the phased array applicator surrounding the segmented phantom visualized on the xy plane; the reported number are used to index the antennas of the array; the tumor target (T1) is highlighted in green. **d** Visualization of the segmented tissues in the region of interest (ROI) on the yz (top) and xz (bottom) planes passing through the tumor at its centroid. **e** Perspective and side view of the 5th patch antenna with the optimized geometrical parameters. **f** Optimized reflection coefficient: a bandwidth (-10 dB) of about 30 MHz is achieved around the central frequency (434 MHz) (dashed line). Source data are provided as a Source Data file.

As shown in Supplementary Figs. 1a-d, we simulated a hyperthermia (HT) treatment in the neck of the phantom, where we inserted a tumor mass with non-uniform shape, placed in the laryngotracheal region (Supplementary Figs. 1b-d). The overall dimensions of the tumor target are reported in Supplementary Fig. 1b, while the coordinates of its centroid with respect to the considered reference system are $x_c = 18.02$ mm, $y_c = 16.15$ mm, and $z_c = 1574.9$ mm. The dielectric properties, i.e., the effective conductivity σ (S m^{-1}) and the real relative permittivity ε_r, at the operating frequency $f = 434$ MHz, have been assigned to the different tissues of the phantom according to the IT'IS database[6]; for the tumor tissue, the properties have been set to the values[7]: $\varepsilon_r = 59$, $\sigma = 0.89$ S m^{-1}.

The considered HT applicator is a uniform circular array made of $N_a = 8$ patch antennas (Supplementary Figs. 1a, 1c), properly optimized in Sim4Life to operate in the water bolus and resonate at the operating frequency $f = 434$ MHz. With reference to Supplementary Fig. 1e, the optimized dimensions of each antenna are: $L_p = 31.0$ mm, $W_p = 7.2$ mm, $L_{gr} = 50$ mm, $W_{gr} = 40$ mm, $h_p = 8.4$ mm and $x_f = 4.96$ mm, being the last element the distance of the feeding point to the

edge of the patch. The position of the antenna array with respect to the Duke model and the tumor is shown in Supplementary Figs. 1a, 1c. The reflection coefficient of the optimized antenna element, simulated as part of the entire array, shows a bandwidth (-10 dB) of about 30 MHz around the operating frequency (434 MHz) (see Supplementary Fig. 1f), proving to be sufficient for the purposes of the presented simulation study.

To find the antenna feeding coefficients that maximize the heating in the tumor region, we followed the approach described in the Supplementary Note 1, and we minimized the function 1/THQ (see Eq. S4) with the particle swarm optimization (PSO) algorithm provided by MATLAB[8]. The algorithm required 13.7 thousand iterations and 39 min to reach the convergence on an Intel Core i7-7700 workstation, with 64 GB RAM, providing the coefficients listed in Supplementary Table 1. The simulated SAR distribution in the ROI corresponding to the optimized set of phases and amplitudes is shown in Supplementary Fig. 2 for a total input power $P_0 = 52$ W (see Eq. (S3)). As can be observed, a good SAR focusing is achieved in correspondence of the tumor region; the hotspots near the skin do not represent an issue, since their effect will be thermally mitigated by the cooling action of the water bolus.

To visualize the effects of the microwave heating in terms of temperature rise, the optimized SAR distribution is used as source term of the bioheat equation, initial and thermal boundary conditions are enforced on the model's boundaries[9], and thermal parameters are assigned to the different tissues in the ROI (Methods, main article). However, thermal parameters, like perfusion, are known with significant uncertainties, which can affect the resulting temperature map in the ROI and lead to unreliable temperature predictions. The characteristics of the implemented in-silico testbed, designed following the ESHO guidelines[10], are summarized in Supplementary Table 2.

Supplementary Table 1 | In-silico testbed: optimized antenna amplitudes and phases for the tumor placed in position T1 for the phantom Duke V3.0

n	1	2	3	4	5	6	7	8
ν_n $(-)$	0.70	0.90	0.90	1.00	0.83	0.74	0.10	0.90
φ_n (°)	-46.27	-31.21	0.01	51.10	84.70	86.33	77.15	26.90

The numbering of the antennas is reported in Supplementary Fig. 1c.

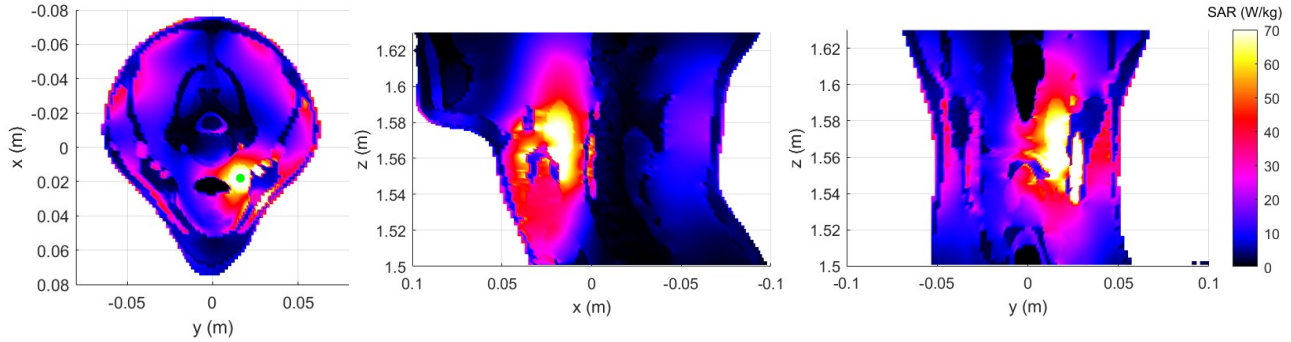

Supplementary Fig. 2 | In-silico testbed: optimized SAR maps for the phantom Duke V3.0. Optimized SAR distribution simulated in Sim4Life[4] and displayed on the three canonical planes passing through the tumor target at its centroid. The corresponding antenna feeding coefficients are reported in Supplementary Table 1, and the total input power of the array is fixed at $P_0 = 52$ W. The green dot on the SAR distribution displayed on the xy plane indicates the position T1 (Supplementary Fig. 1c) of the tumor's centroid. Source data are provided as a Source Data file.

Supplementary Table 2 | In-silico testbed: characteristics of the model

Characteristic	Description
HT application	H&N deep-seated tumors
Patient models	Ella cV3.0 and Duke V3.0[4,5] with tumor insertion (detailed anthropomorphic models with accurate anatomical resolution and tissues – including tumor tissue[10])
Applicator	Circular array of patch antennas, mimicking the HYPERcollar applicator, designed to work in the waterbolus at 434 MHz
Simulation software	Sim4Life v7.0.2, Zurich MedTech, Zurich, Switzerland[4]
EM-simulation method	Finite-difference time-domain (FDTD)
Maximum mesh grid size	1 mm in the HT applicator, 2 mm in tissue
Baseline properties	IT'IS Foundation tissue properties database[6]
Tumor baseline properties	From literature[7]
Thermal model	Pennes' bioheat equation with the metabolic heat generation source omitted
Patient initial temperature	37 °C
Thermal B.C.	Convective boundary conditions
Feedings optimization	SAR-based optimization Maximization of THQ via the PSO algorithm
Evaluation benchmarks	T50, T90 estimators

In the considered in-silico testbed, the proposed method is applied to mitigate the uncertainty introduced by thermal conductivity (k) and perfusion (ω) of the most relevant tissues in the ROI (i.e., muscle, fat + subcutaneous adipose tissue (SAT), skin and tumor). Assuming the considered thermal parameters to vary in the ranges reported in Table 1 of the main article (in accordance with what is reported in the literature), we decided to sample this parameter space with a Sobol' sequence and to generate $B = 70$ parameter sets $\mathbf{s}_b$, $b = 1, \ldots . . B$. Other parameter sets $\boldsymbol{\xi}_a$ generated from the Sobol' sequence were considered for the creation of the target maps, i.e., the in-silico maps corresponding to sets of parameters that are assumed to be unknown, which we want to reconstruct in the entire ROI using few known temperature values affected by noise. Supplementary Fig. 3 reports a comparison between the temperature map obtained by using the baseline values of the parameters $\mathbf{s}_{\text{base}}$, i.e., $\mathcal{F}(\mathbf{r}, t_{\text{ST}}; \mathbf{s}_{\text{base}})$, and two target maps $\mathcal{F}(\mathbf{r}, t_{\text{ST}}; \boldsymbol{\xi}_a)$, $a = 1, 2$, clearly showing how parameters variation can lead to significantly different temperature predictions in the ROI.

We performed the reconstruction of the considered target maps using L acquisition points $\mathbf{q}_\ell$, $\ell = 1, \ldots, L$, equally distributed along a direction ($\boldsymbol{x}$ or $\boldsymbol{y}$) passing through the tumor's centroid, as depicted in Supplementary Fig. 4b. The reconstructed target maps are obtained with the CLS method (Eqs. (3) and (4) in the main article), using $B = 70$ reconstruction functions and 2000 realizations of Gaussian noise (see Eq. (5) in the main article). For each of the considered cases, the normalized goodness function $g(\chi)$ is reported in Supplementary Fig. 4e when the reconstruction is performed without noise (blue-dot line), and for the different realizations of the Gaussian noise (see the envelope). The curves corresponding to the median and the 95th percentile of the functions $g(\chi)$ evaluated for the different noise realizations are also reported, together with the function $g(\chi)$ obtained by considering the baseline temperature map (red-dot line). As can be observed, for all the considered cases, the curves corresponding to the 95th percentile in Supplementary Fig. 4e indicates that 95% of the ROI has an error lower than 0.9 °C for 95% of the realizations.

To provide a more exhaustive demonstration of the proposed technique, the study reported in Fig. 3c of the main article is performed. To do this, we considered a huge number of cases, including 8 catheters configurations, 10 permutations of 256 elements of a Sobol sequence, such that 70 maps served as reconstruction functions, while the remaining maps were treated as target maps, 100 noise realizations, reproduced for 3 different positions of the tumor target in the phantoms Duke V3.0 and Ella cV3.1, a 26-year-old female body phantom of the Sim4Life virtual population[5] (see Supplementary Fig. 5).

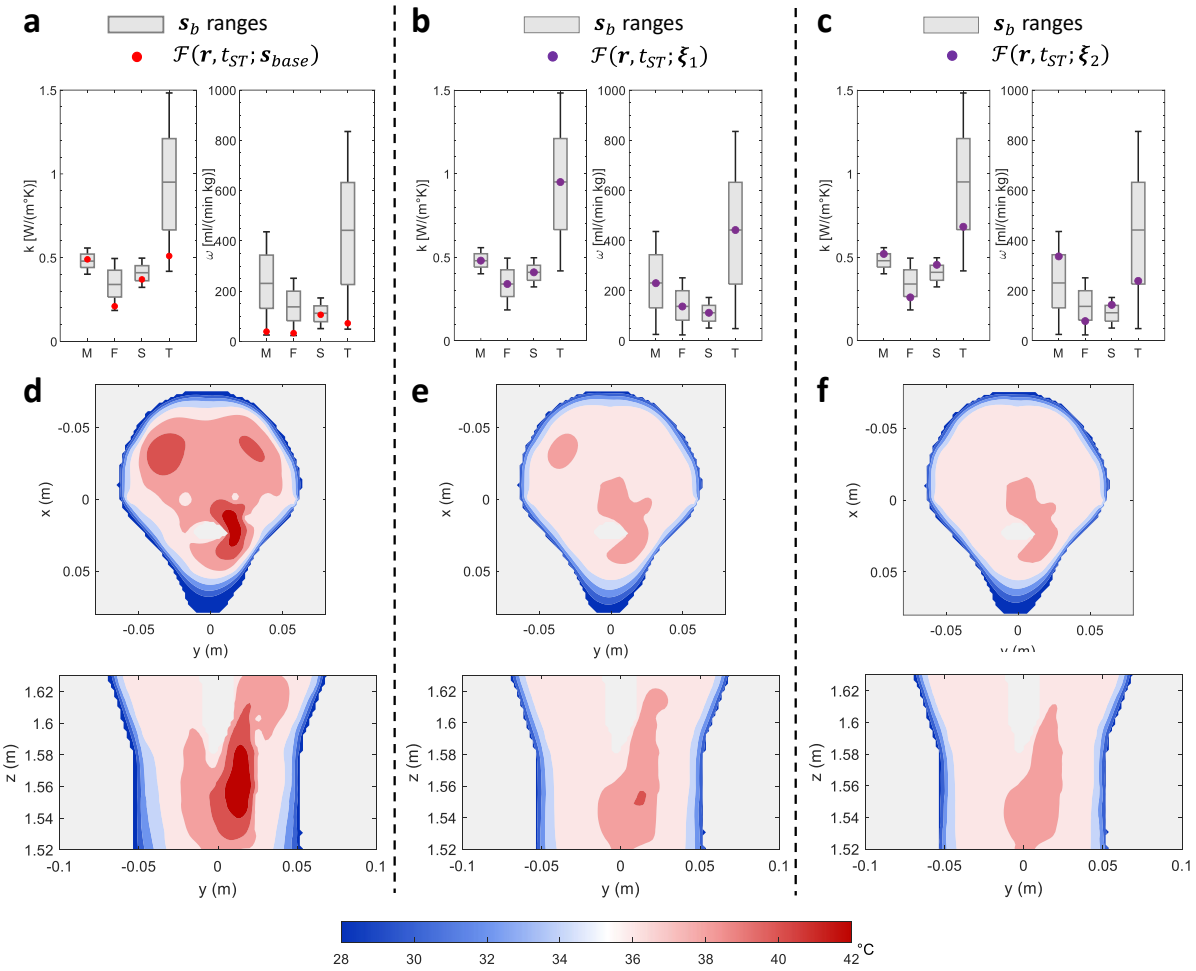

Supplementary Fig. 3 | In-silico testbed: temperature maps variation. a-c Boxplots showing the distribution of the considered sets of thermal parameters (k and ω) of the four most significant tissues in the ROI (i.e., muscle (M), fat + SAT (F), skin (S) and tumor (T)), generated by means of a Sobol' sequence. The overlapping dots show the set of parameters corresponding to the baseline values (a), and two target sets, $\boldsymbol{\xi}_1$ (b) and $\boldsymbol{\xi}_2$ (c). **d-f** Temperature maps displayed on the xy (upper row) and the yz (lower row) planes passing through the tumor at its centroid, corresponding to: (d) the baseline set of parameters; (e) the target set $\boldsymbol{\xi}_1$; (f) the target set $\boldsymbol{\xi}_2$; the temperature distributions are obtained by solving the steady-state bioheat equation (Methods, main article). Source data are provided as a Source Data file.

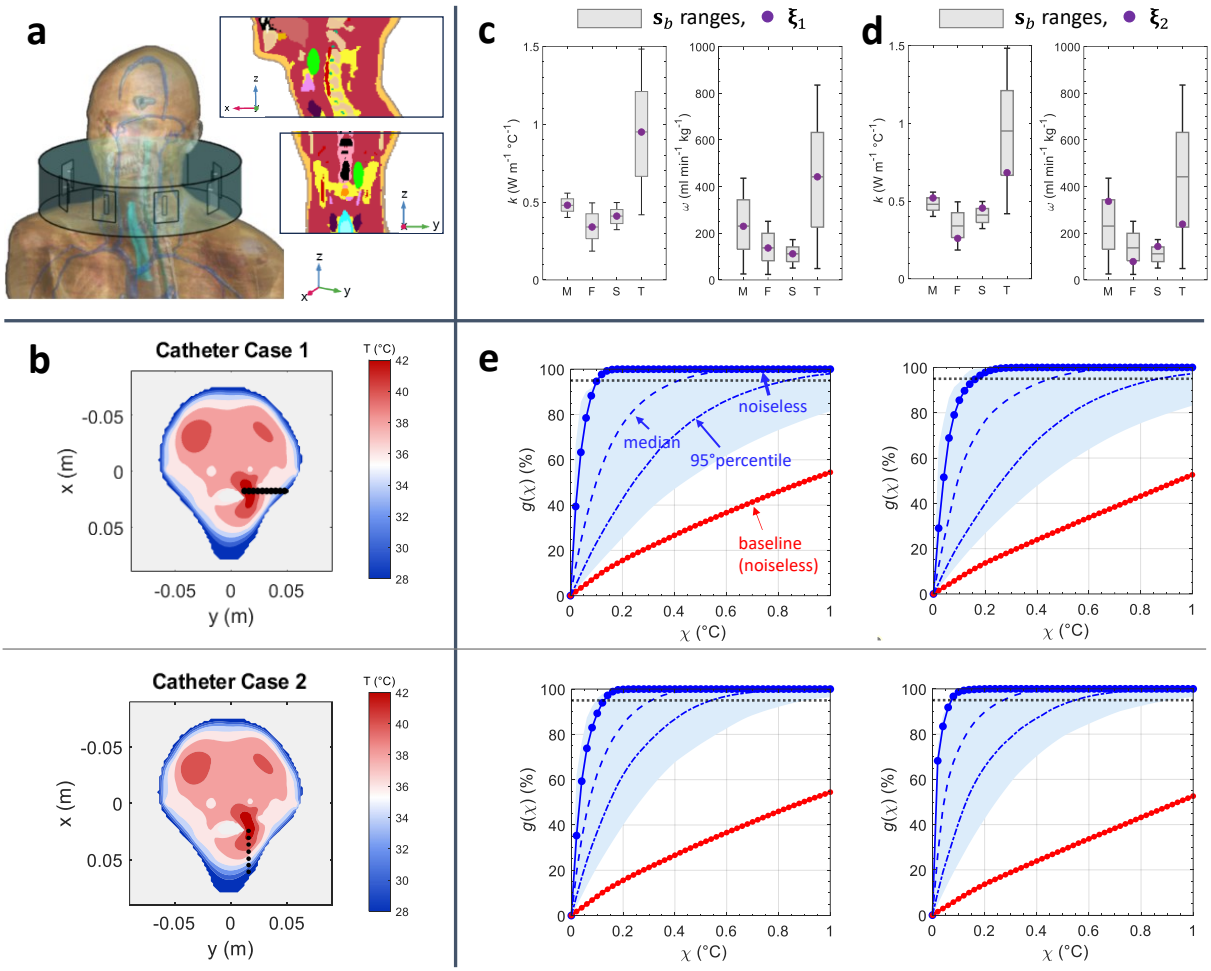

Supplementary Fig. 4 | In-silico testbed results: visualization of the reconstruction error for two target maps and different number of points along the catheter. a Fully anthropomorphic phantom Duke V3.0 employed to simulate an HT treatment, using a phased array applicator made of eight patch antennas immersed in the water bolus; the inset shows the tumor target position T1 (highlighted in green), close to the larynx of the realistic phantom. **b** Different configurations of the acquisition points $\mathbf{q}_\ell$ in the transversal (xy) plane passing through the tumor at its centroid; from top to bottom the number of points considered are: $L = 20$ (case 1) and 7 (case 2); the temperature distribution displayed on the xy plane for illustration purposes corresponds to the baseline map. **c, d** Boxplots showing the minimum, maximum, median and interval between the 25th and the 75th percentiles of the set of thermal parameters (k and ω) corresponding to key tissues in the ROI (M = muscle, F = fat + SAT, S = skin, T = tumor) when a Sobol' sequence is used to sample the parameters space; superimposed blue dots represent the combinations of parameters $\boldsymbol{\xi}_a$ of two target maps, $a = 1$ (c), $a = 2$ (d). **e** Normalized goodness function $g(\chi)$, Eq. (1) in the main article, representing the relative size of the region where the difference between the target maps and the corresponding reconstructed temperature maps is below a certain threshold χ: rows refer to the catheter cases (b), and columns represent the target maps (c, d); the blue-dot line corresponds to the reconstruction of the target map without noise, the blue-shadow region includes 2000 realizations of the Gaussian error $f_{\mathcal{N}}$ (Eq. (5), main article), with $\mu = \pm 0.1$ °C and $\sigma = 0.2$ °C, with the blue dashed line denoting the median and the dash-dotted line indicating the 95th percentile, the red-dot line expresses the discrepancy between the target field and the baseline map (SoA simulation approach). Source data are provided as a Source Data file.

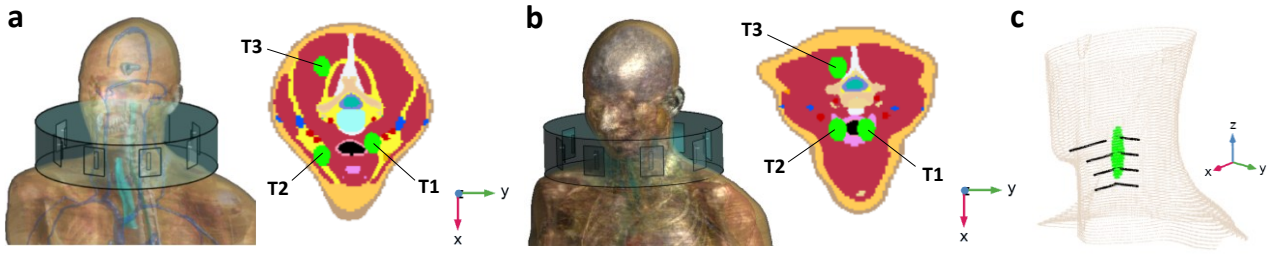

Supplementary Fig. 5 | Fully-anthropomorphic phantoms and target positions. a Fully-anthropomorphic male phantom Duke V3.0 and different positions of the target region displayed on the xy-plane; **b** Fully-anthropomorphic female phantom Ella cV3.1 and different positions of the target region; **c** Candidate catheter positions considered for the single catheter used for the reconstruction, for each tumor position (position T1 in Duke is displayed as an example).

Supplementary Table 3 | In-silico testbed: coordinates of the tumor target centroid

	x_c (mm)	y_c (mm)	z_c (mm)
Duke, T1	18.02	16.15	1574.9
Duke, T2	28.02	-23.85	1574.9
Duke, T3	-41.98	-23.85	1574.9
Ella, T1	3.02	16.15	1424
Ella, T2	3.02	-3.85	1424
Ella, T3	-41.98	-3.85	1424

Supplementary Table 4 | In-silico testbed: optimized antenna amplitudes and phases for the different phantoms and target positions

	n	1	2	3	4	5	6	7	8
Duke, T2	v_n (−)	0.54	0.79	0.74	0.48	0.60	0.68	0.94	0.89
	φ_n (°)	0	130.18	-143.44	-152.53	-163.35	151.14	43.99	0.00
Duke, T3	v_n (−)	0.00	0.60	0.94	0.51	0.86	0.81	0.84	0.48
	φ_n (°)	15.84	-75.03	-125.11	122.32	0.00	0.00	78.52	-131.00
Ella, T1	v_n (−)	0.72	0.65	0.72	0.90	0.82	0.85	0.68	0.69
	φ_n (°)	0.00	-15.81	0.00	59.95	110.50	115.63	88.24	53.69
Ella, T2	v_n (−)	0.43	0.90	0.71	0.96	0.91	1.00	0.79	0.85
	φ_n (°)	0.00	-35.39	0.00	38.46	71.82	63.63	0.00	-14.76
Ella, T3	v_n (−)	0.30	0.63	0.56	0.49	0.54	0.88	0.28	1.00
	φ_n (°)	-151.42	-150.71	164.35	25.64	11.20	35.28	102.67	-175.59

The feeding coefficients for the target position T1 in Duke are reported in Supplementary Table 1.

The coordinates of the tumor targets centroid are reported in Supplementary Table 3 for the considered positions in the two phantoms. For all cases, the overall dimensions of the target were fixed to 16.5 mm along $\hat{\mathbf{x}}$, 13.4 along $\hat{\mathbf{y}}$ and 35.7 mm along $\hat{\mathbf{z}}$. For each of the considered configurations, the SAR-based optimization described in the Supplementary Note 1 was applied, leading to the optimized sets of feeding coefficients reported in Supplementary Table 4. For comparison with Supplementary Fig. 2, the optimized SAR distribution in the ROI for the phantom Ella, when the tumor is located at the position T1, is reported in Supplementary Fig. 6.

To perform the comprehensive analysis reported in Fig. 3 of the main article, 8 catheter positions have been considered for the single catheter used for the reconstruction, for each target position

(Supplementary Fig. 5). Supplementary Table 5 reports the number of sensors along the considered catheters (i.e., the number of acquisition points $\mathbf{q}_\ell$, $\ell = 1, \dots, L$, used in the reconstruction) when a spacing of 6 mm and 2 mm between the sensors is considered, the direction of the catheters (**x** means $y = y_c$, **y** means $x = x_c$, where (x_c, y_c) are the coordinates of the tumor centroid on the xy-plane), and the catheters position along the z-axis with respect to the tumor centroid z-coordinate (z_c).

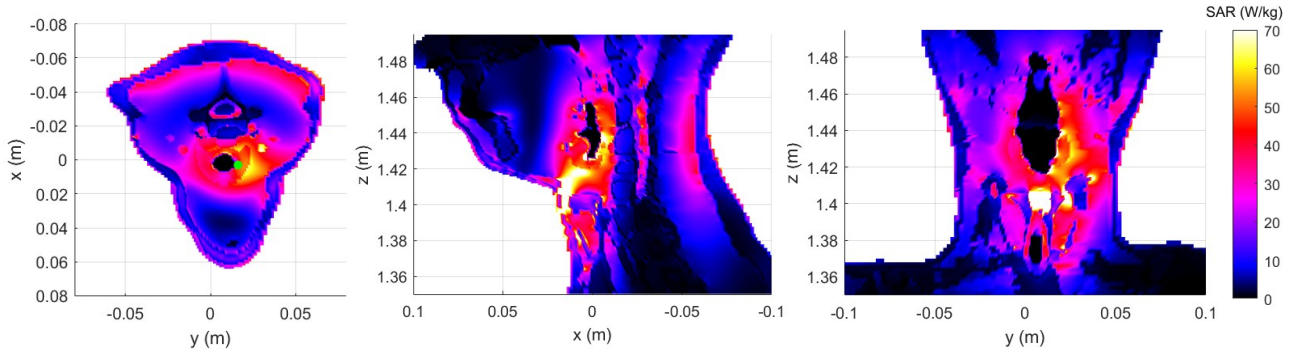

Supplementary Fig. 6 | In-silico testbed: optimized SAR maps for the phantom Ella cV3.1. Optimized SAR distribution simulated in Sim4Life[4] and displayed on the three canonical planes passing through the tumor target T1 at its centroid (Supplementary Table 3). The corresponding antenna feeding coefficients are reported in Supplementary Table 4, and the total input power of the array is fixed at $P_0 = 63$ W. The green dot on the SAR distribution displayed on the xy plane indicates the position T1 of the tumor's centroid. Source data are provided as a Source Data file.

Supplementary Table 5 | In-silico testbed: position and characteristics of the 8 catheters used for each tumor's position

Catheter	Sensors (6mm spacing)	Sensors (2mm spacing)	Direction	z (mm)
1	7	20	**y**	z_c
2	8	23	**x**	z_c
3	7	20	**y**	$z_c + 10$
4	10	30	**x**	$z_c + 10$
5	7	20	**y**	$z_c - 10$
6	6	18	**x**	$z_c - 10$
7	7	20	**y**	$z_c - 20$
8	6	18	**x**	$z_c - 20$

For the transient analysis presented in Fig. 3e and Fig. 3f of the main article, two transient target temperature maps, $\mathcal{F}(\mathbf{r}, t; \text{Model1})$ and $\mathcal{F}(\mathbf{r}, t; \text{Model2})$ were extracted from Sim4Life[4] to demonstrate the robustness of the method when different perfusion models are considered.

The first target $\mathcal{F}(\mathbf{r}, t; \text{Model1})$ is derived from optimized thermal parameters reported in the literature[9], employing a constant perfusion model for each tissue type. The corresponding perfusion values are $\omega = 442.8, 255, 848$ ml kg^{-1} min^{-1}, and thermal conductivities are $k = 0.4, 0.5, 1.5$ W m^{-1} °C^{-1}) for muscle, fat (+SAT), and tumor tissues, respectively. The second target, $\mathcal{F}(\mathbf{r}, t; \text{Model2})$, follows a piecewise linear temperature dependent perfusion model[7,11] for muscle, fat (+SAT), and tumor tissues, as shown in Supplementary Fig. 7a.

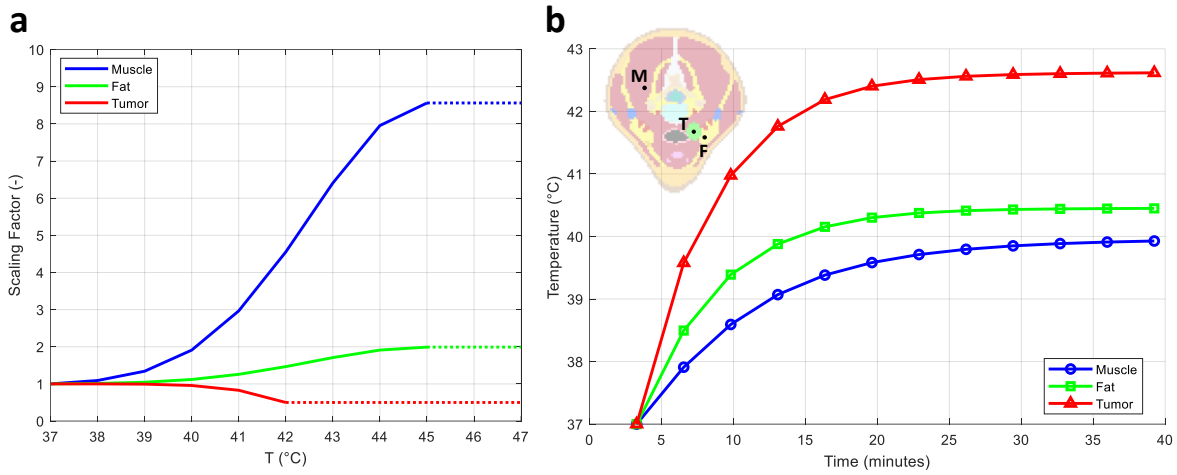

Supplementary Fig. 7 | In-silico testbed: piecewise linear temperature dependent perfusion model. a Perfusion scaling factors used for muscle, fat (+SAT), and tumor. **b** Simulated temperature evolution of the target map $\mathcal{F}(\mathbf{r}, t; \text{Model2})$ in the indicated probe points for the phantom Duke with the tumor in position T1. Source data are provided as a Source Data file.

In this approach, the local perfusion at a given temperature is obtained by multiplying the baseline perfusion at 37 °C ($\omega_0 = 39.1, 32.7, 72.3$ ml kg^{-1} min^{-1}) for muscle, fat (+SAT), and tumor tissues, respectively) with the temperature-dependent scaling factors shown in Supplementary Fig. 7a. Supplementary Fig. 7b presents the temperature evolution of the target map $\mathcal{F}(\mathbf{r}, t; \text{Model2})$ at three distinct probe locations, placed in the muscle, fat (+SAT), and tumor tissues (see the inset).

For the study reported in Figs. 3e, 3f of the main article, we considered the phantom Duke, with the tumor in position T1 (Supplementary Fig. 5a), and we built a library of 140 reconstruction functions $\mathcal{F}(\mathbf{r}, t; \mathbf{s}_b)$ solving the transient Pennes' bioheat equation (see Methods, main article). For each of the two target maps, at 10 evenly spaced times between 6 min and 36 min after the power-on, the reconstruction was performed in 800 cases, obtained by considering 100 noise realizations and 8 catheters configurations with a 6 mm spacing between the sensor points.

Supplementary Note 3 – Experimental testbed detailed description

The structure reproducing the neck in the implemented mock-up is a Poly(methyl methacrylate) (PMMA) cylinder placed centrally with respect to the circular array (see Supplementary Figs. 8a,b); inside the cylinder reproducing the neck, a solid PMMA cylinder (diameter = 45 mm) and a hollow cylinder (outer diameter = 20 mm, inner diameter = 16 mm) are positioned to mimic the presence of the spine and the trachea, respectively (Supplementary Fig. 8b). A system of pipes with flowing water is inserted in the neck cylinder at fixed positions to reproduce the cooling effect of blood flow in the major vessels, i.e., the jugular veins and the carotid arteries.

The neck cylinder is filled with an agar-based phantom, properly developed in our laboratories at Politecnico di Torino to reproduce the dielectric properties of the human muscle at 434 MHz. The phantom is a homogenized mixture of demineralized water, salt, sugar, and agar-agar powder[12,13]; the dielectric properties reported in Supplementary Table 6 are the results of different measurements performed in several experimental sessions during which the agar-based phantom was prepared[13]. The thermal conductivity k and the heat capacity C_p of the muscle phantom reported in Supplementary Table 6 are the weighted averages of two estimations performed independently with different methods and on different samples at the baseline temperature of 37 °C. The first estimation of the thermal properties was carried out at the Department of Applied Science and Technology (DISAT), Politecnico di Torino, using standard methods[14]. The second estimation was performed at

the Department of Energy (DENERG), Politecnico di Torino, with the heat flux meter apparatus Lasercomp FOX600[15] in accordance with the ASTMC518, 1991 standard[16].

The antenna forming the array is a patch antenna with water substrate, where the ground and the patch are printed on layers of I-Tera MT40 ($\varepsilon_r = 3.45$, $\tan\delta = 0.0031$) with thickness 0.508 mm and 0.254 mm, respectively (see Supplementary Fig. 8b). The antenna dimensions have been optimized in CST Microwave Studio[17] in a simplified layered scenario, where the prototype geometry was replaced by finite dielectric layers of water, PMMA and muscle-mimicking phantom material[18]. The distance of the patch antenna from the PMMA layer was fixed to 8 cm, which is approximately twice the minimum distance at which the reflection coefficient becomes stable. The length and the width of the optimized patch antennas were found to be 33.852 mm and 7.126 mm, respectively, the height is 9 mm, and the distance of the feed to the edge is 5.657 mm. The antenna parameters optimized in this simplified layout have been refined by considering the antenna as part of the array in the in-silico counterpart of the prototype realized in the simulation software COMSOL Multiphysics[19] (see Supplementary Fig. 8a). This refinement only resulted in increasing the distance between the antenna ground and the patch element to 10.5 mm. Supplementary Fig. 8c compares the curves of the reflection coefficient evaluated for the single antenna optimized in the simplified layered scenario, the antenna simulated as part of the applicator, and the antenna experimentally realized in the complete hyperthermia mock-up. A good agreement is observed among the different curves, and a bandwidth (-15 dB) of 20 MHz is achieved around the central frequency (434 MHz).

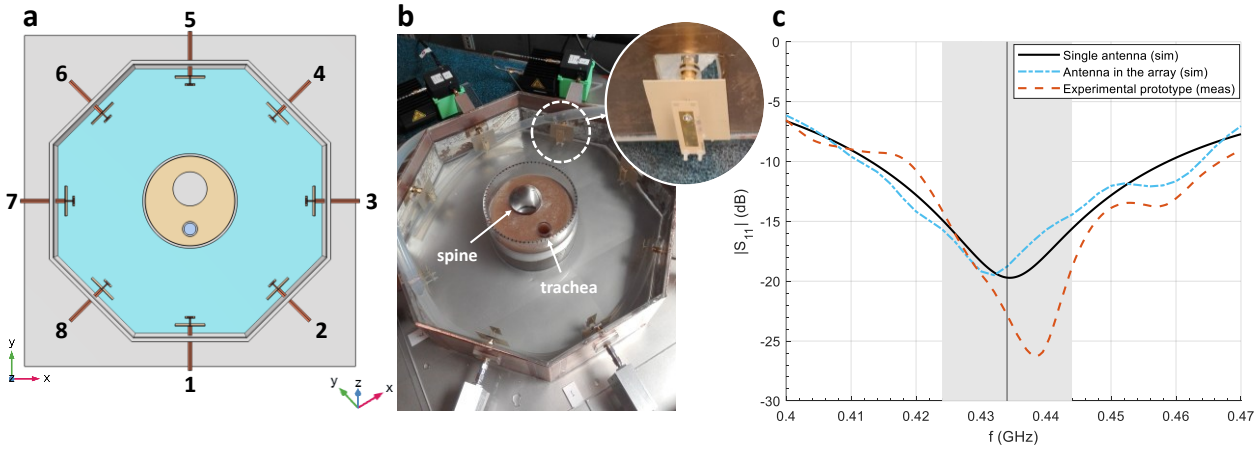

Supplementary Fig. 8 | Experimental testbed: more detailed overview of the HT phased array applicator. a Top view of the experimental prototype simulated in COMSOL Multiphysics; the reported numbers indicate the antennas in the circular array. **b** Top view of the implemented prototype, clearly showing the central phantom reproducing the neck region and the patch antenna forming the array (see the inset). **c** Comparison of the simulated reflection coefficients for the single antenna optimized in the simplified layered scenario and the simulated antenna being part of the 8-elements array with the measurements performed using the experimental prototype. Source data are provided as a Source Data file.

To find the feeding coefficients of the array applicator, the SAR-based optimization procedure described in the Supplementary Note 1 was applied, using the in-silico model of the prototype implemented in COMSOL Multiphysics, where the materials' properties have been assigned according to the values reported in Supplementary Table 6. The SAR was maximized on a spherical region inside the neck phantom with radius r_t = 15 mm, centrally located in the neck along the z-axis ($z_t = 0$ mm) and placed at the spatial coordinates $(x_t, y_t) = (-20, -18)$ mm (being $(0, 0)$ the coordinates of the center of the neck cylinder on the xy plane). For the first demonstration of the mock-up functioning reported in this article, only the antenna phases have been included in the optimization procedure and the resulting values are reported in Supplementary Table 7.

Supplementary Table 6 | Experimental testbed: dielectric and thermal properties of the materials used in the model of the prototype at 434 MHz to perform the SAR-based optimization of the feeding coefficients

Material	ρ (kg m^{-3})	ε_r (−)	σ (S m^{-1})	k (W m^{-1} °C^{-1})	C_p (kJ kg^{-1} °C^{-1})
PMMA	1410	2.33*	1e-4*	0.39	1.4
Water	997	79.53*	0.047*	0.6	4.18
Muscle phantom	1138.27 ± 3.56*	58.09 ± 0.98*	0.91 ± 0.04*	0.50 ± 0.01*	3.20 ± 0.07*

* Weighted averages over different measurements[13]

Supplementary Table 7 | Experimental testbed: optimized antenna phases

n	1	2	3	4	5	6	7	8
φ_n (°)	0	79.83	156.72	-156.06	-142.04	0	-43.86	-43.11

The numbering of the antennas is reported in Supplementary Fig. 8a.

The preparatory stage of the heating session consisted of the following steps: preparation of the sphere used as tumor target; arrangement of the arrays of FBG sensors in the neck container, precisely placing the catheters in the appropriate supports; preparation of the agar mixture reproducing the muscle phantom to be poured into the neck container. Then, after adding the demineralized water in the water bolus, the system was left to rest overnight to reach the thermal equilibrium. The heating session started with setting the phases according to the values reported in Supplementary Table 7; then a total input power $P_0 = 60$ W was uniformly delivered to the system for a total duration of 160 minutes. The way adopted to supply power to the system (uniformly and for about two hours and a half) differs from the clinical practice[1] but was necessary to reach significant temperatures in the target with the available power amplifiers (10 W maximum power per antenna).

To find the ideal simulation model (digital twin) of the implemented prototype, the dielectric properties of the muscle and target phantoms prepared for the specific heating session have been directly measured and are reported in Table 4 (main article). The ideal estimations of the heat transfer coefficients (main article) were instead obtained by varying these parameters in the COMSOL model in order to minimize the average absolute difference between all the measured temperatures and the corresponding simulated values, at all times. Since for all the arrays, the measured focusing peak along the z-axis appears to be coherently shifted downwards with respect to the target's center (see Fig. 4f in the main article) (where the simulations show their peak), a shift $\Delta z = -5$ mm has been introduced in the simulation data corresponding to the ideal model, to account for a possible error in the positioning of the array system.

Supplementary Fig. 9a shows the comparison between the ideal model estimations and the experimental measurements as a function of time, at the target's center z-coordinate ($z = z_t = 0$ mm), for 17 time samples equally distributed from $t_{on} = 0$ min and $t_{off} = 160$ min. Supplementary Fig. 9b reports the same comparison for all the points along each array, at the end time $t = t_{off} = 160$ min . As can be observed, a good agreement is obtained, which allows on one hand to validate the implemented modeling approach, and on the other hand to set a bound on the achievable accuracy when the COMSOL model is used to reproduce the experiment in the best possible (ideal) scenario, i.e. when all the available measurement points are known.

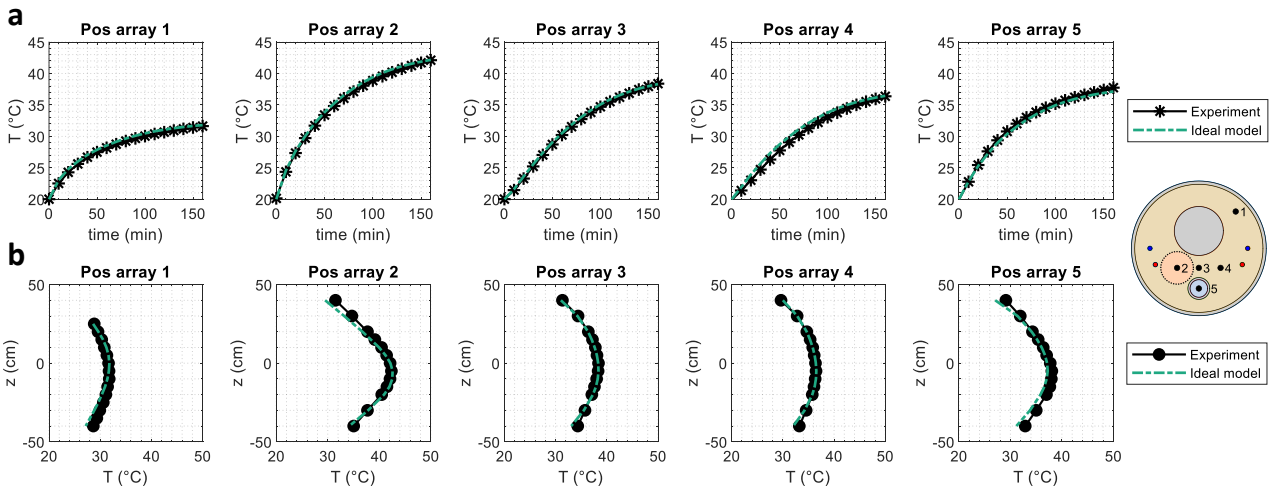

Supplementary Fig. 9 | Experimental testbed: measurements versus ideal simulation model. Measured temperatures and simulated values corresponding to the COMSOL model that best reproduces the experimental mock-up in correspondence of the different arrays' positions (Pos) on the xy-plane, as a function of time at $z = z_t = 0$ mm (**a**), and as a function of the z-coordinate at $t = t_{off} = 160$ min (**b**). Source data are provided as a Source Data file.

The proposed technique is applied in the experimental testbed by considering the temperature information along each array individually to estimate the temperature in all the available points. The library of multiphysics simulations is computed in COMSOL Multiphysics, varying the dielectric properties of the agar-based compounds (Table 4, main article) and the heat transfer coefficients introduced at the different boundaries according to the ranges reported in the main article.

Supplementary Fig. 10 reports the reconstructed temperature profiles along all the available arrays, obtained by applying the constrained least squares (CLS) method to the points of the Array 2 (Supplementary Fig. 10a), placed inside the tumor target, the Array 4 (Supplementary Fig. 10b), and the Array 5 (Supplementary Fig. 10c), at the final time $t = t_{off} = 160$ min. Supplementary Figs. 10a-c also show the available experimental points provided by the FBGs sensors and the temperature profiles corresponding to the ideal simulation model (dash-dotted green curve). A good agreement is observed in all the reported comparisons, even when the reconstruction is performed using the points of the Array 5 (Supplementary Fig. 10c) inserted into the trachea.

To analyze the quality of the reconstruction at different times, the following error metric (ℓ^2-norm) was computed:

$$h(t) = \frac{1}{\sqrt{M}} \left(\sum_{m=1}^{M} \left| \hat{T}(\mathbf{r}_m, t) - \tilde{T}(\mathbf{r}_m, t) \right|^2 \right)^{1/2}, \tag{S5}$$

where $\hat{T}$ is the reconstructed map, while $\tilde{T}(\mathbf{r}_m, t), m = 1, \ldots, M$, indicates all the available experimental points ($M = 66$). The difference reported in Eq. (S5) is the estimator ΔT evaluated at each spatial point and at each time. Expressions similar to Eq. (S5) are obtained by replacing $\hat{T}(\mathbf{r}_m, t)$ with the temperature map corresponding to the ideal simulation model and the reconstruction functions. The results are reported in Supplementary Fig. 11. As can be observed, the errors corresponding to the application of the reconstruction method tend to approximate the errors affecting the ideal model in almost all cases; this demonstrates how the proposed technique is able to provide satisfactory results in real time. The ripple in correspondence of the Array 1 (which is the farthest from the tumor target) is only observed in the initial stage of the heating phase, and the curve tends to stabilize over time, approaching the ideal curve as expected.

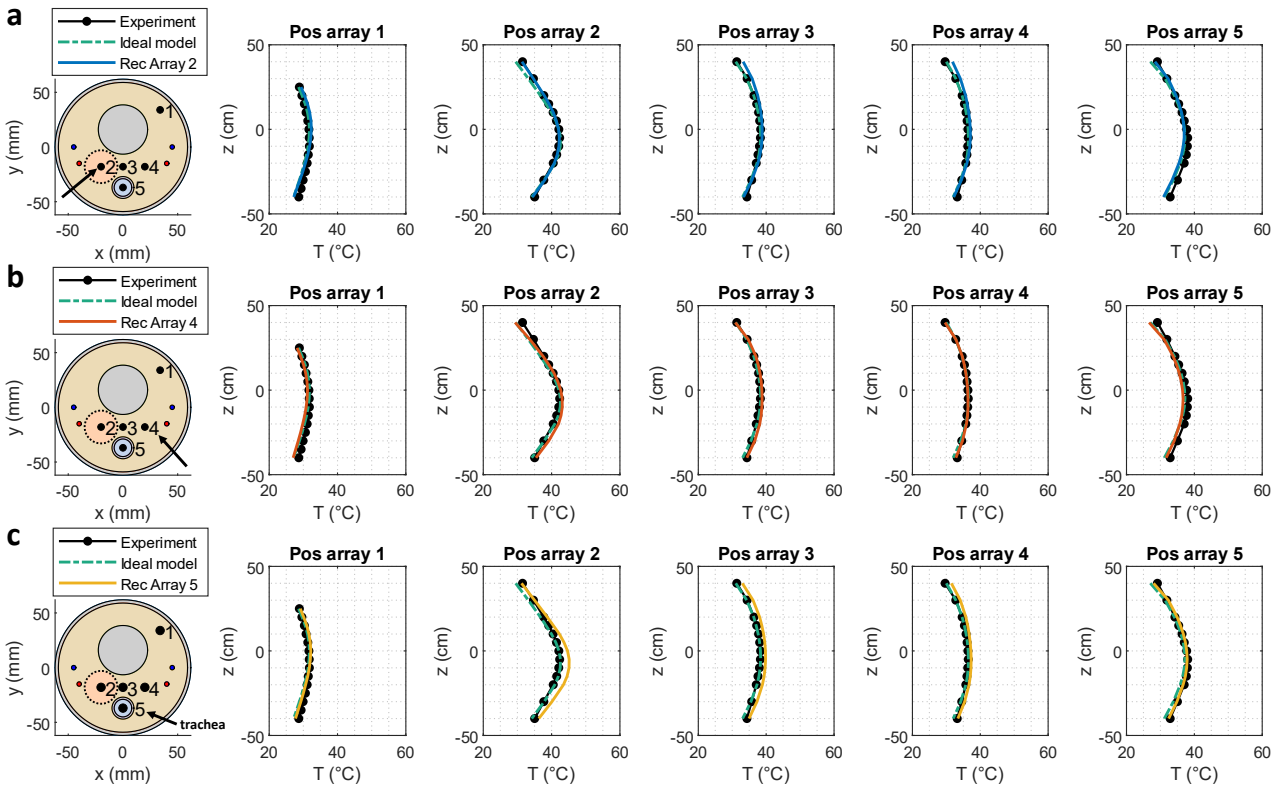

Supplementary Fig. 10 | Experimental testbed results: reconstructed temperature profiles versus experimental values and ideal profiles. Temperature profiles at $t = t_{\text{off}} = 160$ min along all the available arrays at the different positions (Pos) on the xy-plane, reconstructed by applying the CLS method using the experimental points along the Array 2 (**a**), the Array 4 (**b**) and the Array 5 (**c**), where the last one is inserted in the phantom's region mimicking the human trachea. For direct comparison, the measured temperatures are also reported (black-dot line), together with the temperature profiles corresponding to the ideal simulation model (dash-dotted green line), which is the model obtained in COMSOL by directly measuring the dielectric properties of the materials used in the experiment and using heat transfer coefficients derived by fitting the model to all the available experimental data. Source data are provided as a Source Data file.

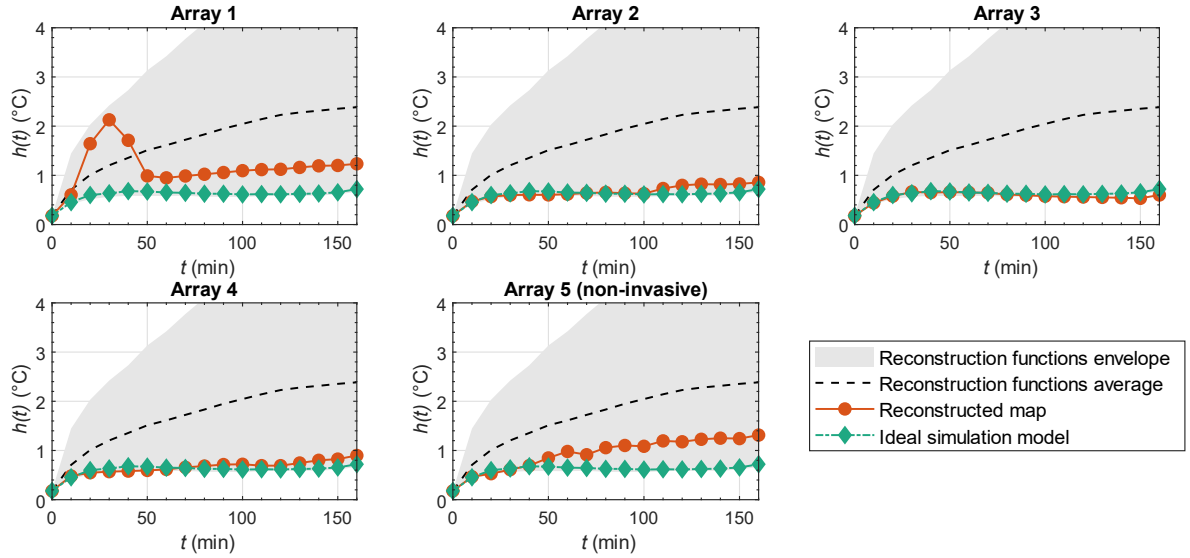

Supplementary Fig. 11 | Experimental testbed results: ℓ^2-norm error $h(t)$ evaluated in all the available points as a function of time. The red-dot lines report the ℓ^2-norm error $h(t)$, Eq. (S5), computed by comparing the reconstructed temperature values and the experimental measurements in all the available points when the reconstruction is performed using the information along the Arrays from 1 to 5, at 17 time samples between the initial and final time of the heating

session. The error is also reported for the ideal simulation model and the reconstruction functions (envelope and average). Source data are provided as a Source Data file.

Supplementary Note 4 – Fiber sensor calibration

The multipoint temperature sensors are basically composed of a dense array of FBGs written in a single fiber embedded in a thin glass capillary. The FBGs have been specifically manufactured for this application writing an array of gratings in a standard SMF-28 fiber using a femto-second laser. Working with standard fibers at around 1550 nm the temperature sensitivity is of about 10 pm but the accurate knowledge of the sensor response with temperature can be only obtained with a proper calibration. To this aim, the overall measurement chain composed of the FBG sensors, the interrogation system and the acquisition and processing system have been calibrated just before the test in order to reduce possible uncertainty contributions related to long-term stability and reproducibility. The calibration setup (see Supplementary Fig. 12a) takes advantage of a temperature sensor calibrator (Fluke 9142 field Dry-Well) and a calibrated temperature sensor to ensure the traceability to the National Standards. A custom made dry-block has been specifically manufactured to host all the capillaries and the reference sensors. The calibrator ensures stability, axial uniformity and radial uniformity better than 0.05 °C and its temperature is measured using a 30cm-long metallic probe which embeds a precision four-wires Pt100 sensor designed to work as secondary reference standard. The sensor was previously calibrated by an independent Calibration Laboratory to ensure traceability. The reference sensor calibration uncertainty was 60 mK (coverage factor $K = 2$).

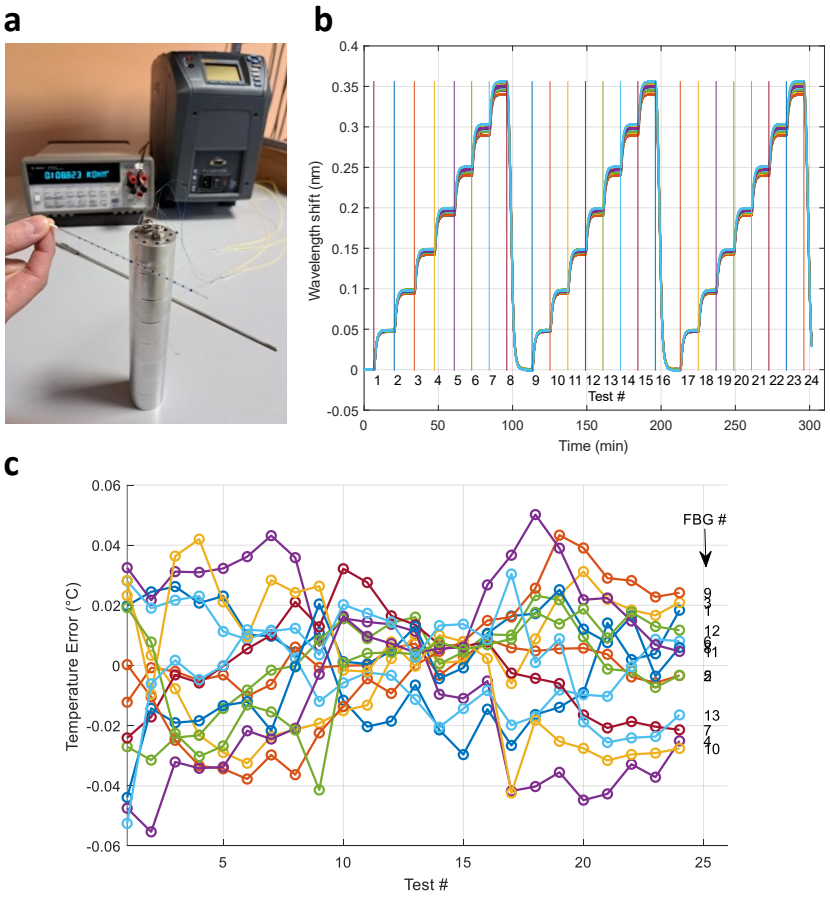

Supplementary Fig. 12 | Experimental testbed: fiber sensor calibration setup and results. a Setup devised for the sensor calibration composed of a programmable dry-well, a reference thermometer, a custom-made dry-block and a 6.5 digits multimeter; the figure also shows a capillary containing an array of 13 FBGs. **b** FBG wavelength shifts recorded during a calibration test; the figure shows the 24 calibration points employed to feed the fitting algorithm. **c** Example of

calibration result: residual temperature errors for each FBG in the array and for each calibration point after the fitting. Source data are provided as a Source Data file.

The calibration was carried out setting the dry-block temperature from 20 °C to 60 °C in progressive steps of 5 °C. The procedure was repeated several times to assess the system repeatability. Supplementary Fig. 12b shows the wavelength shift as recorded during the calibration from one FBG array composed of 13 sensing points. For each step, the temperature was measured at the end of the thermal transient with the reference thermometer using a 6.5 digits multimeter (Agilent 34401A) and the FBG wavelengths were recorded with a commercial FBG analyzer (Luna's Hyperion Si155) thus obtaining, for the test shown in Supplementary Fig. 12b, 24 calibration points.

The calibration curve was obtained for each FBG in the sensor array by fitting a second-order polynomial model. As an example, the residual errors after calibration, for each FBG and for each calibration point, are shown in Supplementary Fig. 12c, where it can be seen that the maximum absolute error does not exceed 60 mK. The overall uncertainty, which includes the fitting uncertainty, the dry-block uniformity, the reference sensor accuracy and the short-term stability (1 day), is of about 0.16 °C (coverage factor $K = 2$).

The effect of the capillary material and dimensions was investigated by the authors in a previous work[20], where it was shown that the capillary introduces a temperature error that depends not only on the physical properties but also on the thermal gradient. Specifically, under uniform temperature conditions, the capillary does not cause any distortion in the temperature distribution. However, when the capillary has a thermal resistance different from the surrounding material, it introduces an error proportional to the gradient. The results reported in Supplementary Fig. 10 show a difference among measurements obtained during the experiments, temperature obtained through the ideal model and temperatures reconstructed by applying the CLS method that are not directly related to the gradient, thus highlighting that the capillary dimensions and material do not seem to have a major influence on the observed discrepancies.

Supplementary References

1. Rijnen, Z. et al. Clinical integration of software tool VEDO for adaptive and quantitative application of phased array hyperthermia in the head and neck. *Int. J. Hyperthermia* **29**, 181–193 (2013).
2. Rijnen, Z. et al. Quality and comfort in head and neck hyperthermia: A redesign according to clinical experience and simulation studies. *Int. J. Hyperthermia* **31**, 823–830 (2015).
3. Canters, R. A. M., Wust, P., Bakker, J. F. & van Rhoon, G. C. A literature survey on indicators for characterisation and optimisation of SAR distributions in deep hyperthermia, a plea for standardization. *Int. J. Hyperthermia* **25**, 593–608 (2009).
4. Sim4Life, version 7.0.2. https://zmt.swiss/sim4life/ (2022).
5. Gosselin, M. C. et al. Development of a new generation of high-resolution anatomical models for medical device evaluation: the Virtual Population 3.0. *Phys. Med. Biol.* **59**, 5287–5303 (2014).
6. Hasgall, P. A. et al. IT'IS database for thermal and electromagnetic parameters of biological tissues. [Online] Available: http://www.itis.ethz.ch/database (2018).
7. Drizdal, T., Paulides, M. M., van Holthe, N. & van Rhoon, G. C. Hyperthermia treatment planning guided applicator selection for sub-superficial head and neck tumors heating. *Int. J. Hyperthermia* **34**, 704–713 (2018).
8. MATLAB. Natick, Massachusetts: The MathWorks Inc. (2023).

9. Verhaart, R. F. et al. Accurate 3D temperature dosimetry during hyperthermia therapy by combining invasive measurements and patient-specific simulations. *Int. J. Hyperthermia* **31**, 686–692 (2015).
10. Paulides, M. M. et al. ESHO benchmarks for computational modeling and optimization in hyperthermia therapy. *Int. J. Hyperthermia* **38**, 1425–1442 (2021).
11. Lang, J., Erdmann, B. & Seebass, M. Impact of nonlinear heat transfer on temperature control in regional hyperthermia. *IEEE Trans. Biomed. Eng.* **46**, 1129–1138 (1999).
12. Hartsgrove, G., Kraszewski, A. & Surowiec, A. Simulated biological materials for electromagnetic radiation absorption studies. *Bioelectromagnetics* **8**, 29–36 (1987).
13. Gaffoglio, R. et al. Highly reproducible tissue-mimicking phantoms for hyperthermia applications. *AP-S/URSI* (2024).
14. Standard Test Method for Determining Specific Heat Capacity by Differential Scanning Calorimetry. ASTM E1269-11 (2018).
15. Lorenzati, A., Fantucci, S., Capozzoli, A. & Perino, M. VIPs thermal conductivity measurement: Test methods, limits and uncertainty. *Energy Procedia* **78**, 418–423 (2015).
16. Standard Test Method for Steady-State Heat Flux Measurements and Thermal Transmission Properties by Means of the Heat Flow Meter Apparatus. ASTM International C518-91 (1991).
17. CST Studio Suite. Dassault Systèmes Simulia. www.cst.com (2022).
18. Paulides, M. M., Bakker, J. F., Chavannes, N. & van Rhoon, G. C. A patch antenna design for application in a phased-array head and neck hyperthermia applicator. *IEEE Trans. Biomed. Eng.* **54**, 2057–2063 (2007).
19. COMSOL Multiphysics, version 6.1. www.comsol.it (2023).
20. Gassino, R., Vallan, A. & Perrone, G. Evaluation of temperature measurement errors due to FBG sensors during laser ablation of Ex-Vivo porcine liver. *IEEE International Instrumentation and Measurement Technology Conference*, 1–5 (2018).